Crystal structure and antiferromagnetic spin ordering of $LnFe_{2/3}Mo_{1/3}O_3$ (Ln = Nd, Pr, Ce, La) perovskites

S. A. Ivanov,[1,2] P. Beran,[3] G. V. Bazuev,[4] T. Ericsson,[5] R. Tellgren,[5] P. Anil Kumar,[2] P. Nordblad,[2] and R. Mathieu[2,*]

[1]*Center of Materials Science, Karpov' Institute of Physical Chemistry, Moscow 105064, Russia*

[2]*Department of Engineering Sciences, Uppsala University, Box 534, 751 21 Uppsala, Sweden*

[3]*Nuclear Physics Institute ASCR, Rez, Czech Republic*

[4]*Institute of Solid-State Chemistry, Ural Branch of the Russian Academy of Science, 620999 Ekaterinburg, GSP-145, Russia*

[5]*Department of Chemistry–Ångström Laboratory, Uppsala University, Box 538, 751 21 Uppsala, Sweden*

(Received 16 December 2014; revised manuscript received 5 March 2015; published 17 March 2015)

Stoichiometric polycrystalline samples of $LnFe_{2/3}Mo_{1/3}O_3$ (Ln = Nd, Pr, Ce, La) have been prepared by solid-state reaction and studied by means of x-ray and neutron powder diffraction as well as Mössbauer spectroscopy and magnetic measurements. All samples were found to be of single phase and to have *Pnma* symmetry with valence state +3 of Fe and Mo. It is demonstrated that the *B*-site cations of $LnFe_{2/3}Mo_{1/3}O_3$ in accord with $LnFeO_3$ order in a G-type antiferromagnetic structure with the magnetic moments aligned along the *b* axis. However, with significantly lower Néel temperatures than their $LnFeO_3$ parent compounds. The Fe-O-Fe bond lengths and bond angles and thus the magnitude of the antiferromagnetic superexchange interaction are found to systematically change with the ionic radius of Ln such that T_N increases with increasing radius. Only the $CeFe_{2/3}Mo_{1/3}O_3$ compound experiences a low temperature spin reorientation from alignment along the *b* axis to the *a* axis.

DOI: 10.1103/PhysRevB.91.094418 PACS number(s): 75.47.Lx, 75.30.Et, 61.05.fm

I. INTRODUCTION

Complex metal oxides with perovskite-type structure provide a rich set of electronic, magnetic, and structural order [1–6], and, e.g., orthoferrites are considered attractive for industrial applications such as cathode material for fuel cells, thermoelectric power conversion, oxygen permeable membranes, gas sensors, and advanced information storage [7–10]. Rare-earth orthoferrites $LnFeO_3$ are of special interest due to coexistence of weak ferromagnetism and dipole ordering where the spontaneous polarization is directly coupled to the magnetic order [11–14].

$LnFeO_3$ compounds order antiferromagnetically with Néel temperatures, T_N, ranging from 620 to 740 K [15–19]. These ordered states include canted antiferromagnetism, spin reorientations, compensation effects, and ordering of the Ln^{3+} cation moments at low temperatures [20–23]. The magnetic cations in the A and B sites order in two interspersed simple cubic sublattices due to different interaction pathways: Fe–Fe, Ln–Fe, and Ln–Ln. At lower temperature the competition between the Fe–Fe and Ln–Fe interactions can lead to a spin-reorientation transition of the ordered Fe^{3+} magnetic moments [24–28]. Due to the weak Ln–Ln interaction the Ln spins order only at very low temperature [18]. From symmetry conditions rare-earth orthoferrites are also expected to be ferroelastic [29–31].

The magnetic properties of rare-earth orthoferrites may further be altered and tuned by substitution of Fe with other $3d/4d$ elements. The effect of substitution with nonmagnetic ions is significant even for small concentrations [32]. In this paper one-third of the Fe^{3+} cations are substituted with Mo^{3+} cations to form $LnFe_{2/3}Mo_{1/3}O_3$ giving rise to a mixed spin system on the B site. Since Mo^{3+} cations (0.69 Å) are slightly larger than the high-spin Fe^{3+} (0.645 Å), the lattice parameter values and the unit cell volume only slightly increase with Mo doping and $LnFe_{2/3}Mo_{1/3}O_3$ retains the same *Pnma* structure type as the nonsubstituted parent compounds. Detailed studies of the temperature evolution of the nuclear and magnetic structure and the magnetization of stoichiometric samples of $LnFe_{2/3}Mo_{1/3}O_3$ (Ln = Nd, Pr, Ce and La) are reported.

II. EXPERIMENTAL PROCEDURE

The synthesis of pure and stoichiometric samples is critically important. The target orthoferrites are metastable phases at high temperatures compared with the thermodynamically stable $Ln_3Fe_5O_{12}$ garnet and Ln_3MoO_7 phases [33]. Ceramic samples of $LnFe_{2/3}Mo_{1/3}O_3$ (Ln = Nd, Pr, Ce, La) were prepared under vacuum following the specific procedure proposed by Bazuev *et al.* in Refs. [34,35], using stoichiometric amounts of starting reactants, the binary oxides La_2O_3, CeO_2, Pr_2O_3, Nd_2O_3, Fe_2O, and MoO_3 and Mo metal. The phase purity and the structure of the intermediate and final powder samples was checked from x-ray powder diffraction (XRPD). See the Supplementary Material for more details on synthesis conditions and experimental methods [36].

The chemical composition of the prepared ceramic samples was analyzed by energy-dispersive spectroscopy (EDS) using a JEOL 840A scanning electron microscope and INCA 4.07 (Oxford Instruments) software. Analyses performed on several particles showed that the concentration ratios of Ln/Fe/Mo were the stoichiometric ones within the instrumental resolution (see Table I). The oxygen content of the prepared samples was determined iodometrically. Several runs of the iodometric titrations were performed on each sample, both before and after intermediate XRPD measurements at low temperatures (T = 10 K), with similar results. Any oxygen nonstoichiometry was reliably found confined within a frame of –0.008(4) to +0.005(3).

An MPMSXL SQUID magnetometer and a PPMS6000 system with VSM option, both from Quantum Design Inc., were

*roland.mathieu@angstrom.uu.se

TABLE I. Lattice parameters and associated volume V for $Ln Fe_{2/3}Mo_{1/3}O_3$ samples refined at room temperature using X-ray powder diffraction data (s.g. *Pnma*). Ionic radii r and tolerance factor t are added for reference, as well as the Ln/Fe/Mo ratios estimated from EDS.

Phase	Nd	Pr	Ce	La
r(c.n. = 8)	1.109	1.126	1.143	1.16
t	0.876	0.886	0.891	0.900
a,Å	5.6785(1)	5.6700(1)	5.6528(1)	5.6505(1)
b,Å	7.8154(1)	7.8424(1)	7.8738(1)	7.9227(1)
c,Å	5.4743(1)	5.5085(1)	5.5467(1)	5.5861(1)
V, Å^3	242.95(1)	244.94(1)	246.87(1)	250.08(1)
Ln/Fe/Mo (EDS)	1.01/0.67/0.32	1.02/0.65/0.33	1.01/0.65/0.34	0.99/0.68/0.33

used for the magnetization measurements. The magnetization was recorded as function of temperature in zero-field-cooled and field-cooled protocols in the temperature ranges 5–320 K and 300–700 K, and magnetic hysteresis loops were recorded at different temperatures in fields up to 7 T.

The transmission Mössbauer spectrometer was of constant acceleration type, using 1024 cells for storing the unfolded data. The source, ^{57}CoRh, was always held at room temperature. The absorbing material, typically around 25 mg/cm^2, was crushed and mixed with a suitable amount ($\approx$ 50 mg/cm^2) of boron nitride and spread evenly over the absorber disk, diameter 13 mm. The amount of material was chosen to give maximum signal-to-noise ratio [37]. The folded spectra (512 cells) covering a velocity span of $\pm$12 mm/s were least-squares fitted using the RECOIL program [38]. The center shift (CS), being the sum of the true isomer shift and the second-order Doppler shift, is given relative to metallic iron at room temperature.

Neutron powder diffraction (NPD) patterns were performed on the diffractometer MEREDIT@NPI (Rez, Czech Republic), using a neutron wavelength of 1.46 Å [Cu(220) monochromator]. Data were collected between 4° and 144° in 2θ with steps of 0.08° at four temperatures (4, 295, 450, and 600 K). The diffraction patterns were analysed using the FULLPROF program [39]. The refined atomic coordinates were used to calculate the magnitude of the tilting angles [40,41]. From individual bond distances the valences of cations were calculated at room temperature following the bond valence sum (BVS) method [42,43]. This phenomenological model gives estimates of the valences on the cations by means of an empirical relationship between the observed bond lengths and the valence of the connected ions. The IVTON software [44] was employed to characterize the coordination spheres and valence states of the A- and B-site cations and to obtain bond lengths, volumes of the coordination polyhedra, and the displacements of the cations from the centers of these. The magnetic structure was refined as an independent phase in which only Fe^{3+} cations were included. Magnetic symmetry analysis was then done using the program BASIREPS, also part of FULLPROF [39]. Several magnetic models proposed by BASIREPS were tried in the refinement and the final structure model was selected on the basis of agreement factors and stability of the refinement.

III. RESULTS

A. Sample characterization

As mentioned above, the EDS elemental analyses and the iodometric titrations showed that the composition of the $Ln Fe_{2/3}Mo_{1/3}O_3$ samples was close to the nominal. Scanning electron micrographs indicated a uniform distribution of grains (average size 30–40 nm) and the results from the second harmonic generation (SHG) measurements indicated a centrosymmetric state of all samples at room temperature.

B. XRPD studies

Initial XRPD analyses of the room-temperature diffractograms showed that the samples formed powders with perovskite structure (see Fig. 1) and that all $Ln Fe_{2/3}Mo_{1/3}O_3$ (Ln = Nd, Pr, Ce, La) samples had the expected orthorhombic (*Pnma*) symmetry without any ordering of Fe and Mo in the B sublattice. Comparison of diffraction patterns of $Ln Fe_{2/3}Mo_{1/3}O_3$ and $Ln FeO_3$ [45] show that the peaks of the doped samples are systematically shifted to lower diffraction angles supporting the replacement of Fe^{3+} by Mo^{3+} in the B site. The XRPD patterns were refined by the Rietveld method and the final plots indicate that each sample is single phased with no detectable impurities. The observed and calculated (the final Rietveld plots) XRPD patterns are both displayed in Fig. 1. In all cases, the structure was refined in the orthorhombic space group *Pnma* with $z = 4$ (number of formula units), with unit-cell parameters related to the ideal cubic perovskite, $a_0 \approx 3.8$ Å, as $a \approx c \approx \sqrt{2}a_0$, $b \approx 2\,a_0$. The *Ln* cations were located at the 4*c* positions, Fe and Mo at 4*b*, and the oxygen atoms at 4*c* and 8*d* positions, respectively. The lattice parameters and associated cell volumes are collected in Table I (see Table S1 in the Supplemental Material [36] for atomic positions and occupations, as well as reliability factors). The refined lattice parameters are in reasonable agreement with values reported previously in Refs. [34,35]. The A- and B-site occupancies were refined to check the cation stoichiometry and the refined occupancies were found to be consistent within the standard deviation from the expected values. Therefore, the cation occupancies were fixed to the stoichiometric ratios to avoid strong correlation with the displacement parameters.

C. Magnetic properties

The temperature dependence of the magnetization of the compounds, measured in zero-field-cooled (ZFC) and field-cooled (FC) conditions from room temperature to 700 K, is shown in the left panels of Fig. 2. The magnetization curves suggest antiferromagnetic (AFM) transitions for all compounds, albeit at significantly lower T_N than their Mo-free counterparts.

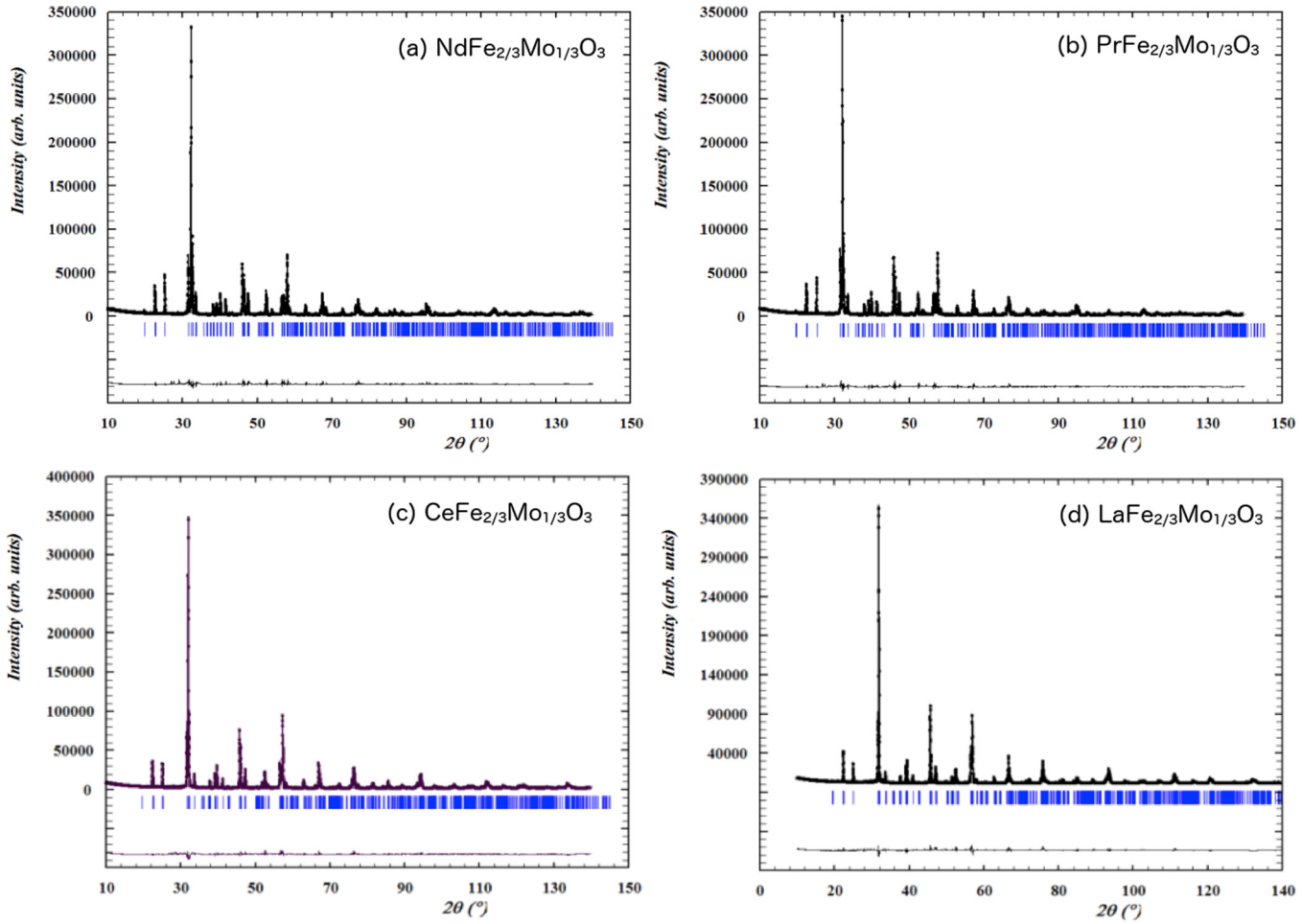

FIG. 1. (Color online) Rietveld refinement of XRPD data for $Ln\mathrm{Fe}_{2/3}\mathrm{Mo}_{1/3}\mathrm{O}_3$ perovskites (Ln = Nd (a), Pr(b), Ce(c), La(d)). The upper traces illustrate the observed data as dots, and the calculated pattern as solid line; the lower solid trace is a plot of the difference, observed intensity minus the calculated one. The tick marks show positions calculated for Bragg reflections.

Irreversibility is observed in the ZFC/FC curves of all the Mo-doped samples, reflecting the imperfect compensation of the magnetic moments in the antiferromagnetic structure established below T_N.

Mo-free LnFeO3 systems (Ln = Nd, Pr, Ce, La) undergo antiferromagnetic transitions at high temperatures, around 700 K [18,19]. Here in the Mo-doped samples, T_N decreases with decreasing Ln cation size, from about 490 K in the Ln = La case down to about 470 K for Ln = Nd. Some irreversibility is observed in the magnetization curves of the Nd compound above T_N, possibly reflecting the presence of minute amounts of a secondary phase or Fe/Mo segregation or disorder [46,47]. As seen in the magnetization-versus-magnetic field curves shown in the right panels of Fig. 2, the magnetization of all compounds increases linearly with the magnetic field at high magnetic fields. At lower fields it displays some hysteresis, most evident in the case of Ln = Pr, whose magnetization curves are reminiscent to those of LaFeO_3 [19]. In earlier studies of undoped $Ln\mathrm{FeO}_3$ samples (Ln = Nd, Pr, Ce, La) it was argued that in addition to AFM ordering at high temperatures, some compositions (with Ln = Ce and Nd) undergo a spin reorientation at 240 K and 190 K [24–28]. Low-temperature ZFC- and FC-magnetization curves have been recorded for all compounds and are plotted in Fig. 3(a). The curves obtained for the Nd compound only show a weak irreversibility below 160 K. However, a sharp step is observed in the case of the Ce compound below about 70 K. No such anomalies were observed in the magnetization curves of the La and Pr samples. The switch is observed for the $\mathrm{CeFe}_{2/3}\mathrm{Mo}_{1/3}\mathrm{O}_3$ in both the ZFC and the FC curves and suggests a reorganization of the magnetic structure yielding a lower magnetization at low temperatures. Magnetization versus magnetic field curves were collected at temperatures above 5 K [see Fig. 3(b)]. For this compound, the hysteresis loop at 100 K shows a much larger coercivity than the one at 5 K.

D. Mössbauer spectroscopy

Mössbauer spectra of all $Ln\mathrm{Fe}_{2/3}\mathrm{Mo}_{1/3}\mathrm{O}_3$ samples were measured at room temperature. All obtained spectra were very similar and could be well fitted using magnetic sextets. However, the spectra were not symmetric, e.g., the left profile (most negative velocity, number "1") was always broader but not as deep as the right one (most positive velocity, number "6"). The area of profile 1 was the same as the area of profile 6, however. Similar observations could be done for profile numbers 2 to 5. To simulate the observed broadenings, three

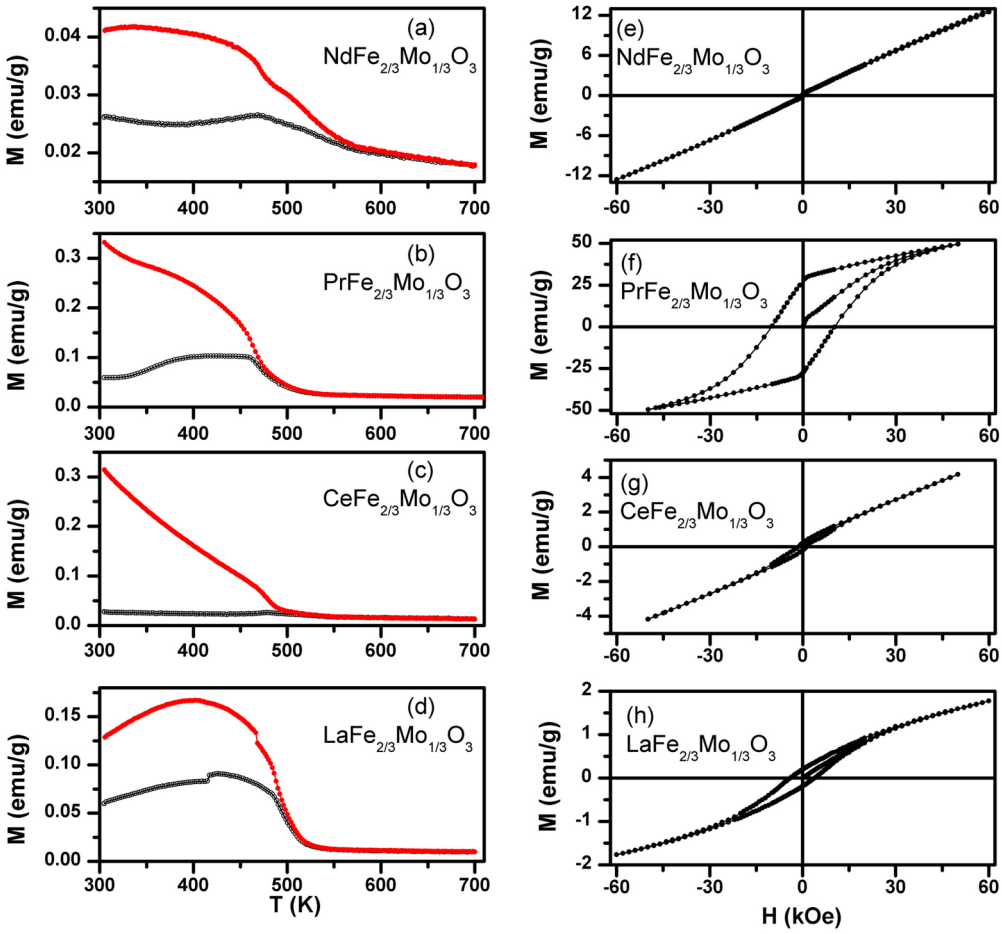

FIG. 2. (Color online) (left panels) Field-cooled (FC, in red (gray)) and zero-field-cooled (ZFC, in black) magnetization curves recorded under a magnetic field H = 1 kOe and (right panels) magnetic field dependence of the magnetization at T = 5 K for the different perovskites $Ln\mathrm{Fe}_{2/3}\mathrm{Mo}_{1/3}\mathrm{O}_3$ with *Ln* = Nd (a, e), Pr (b, f), Ce (c, g), La (d, h).

Mössbauer sextets were used in the fittings where the outer peaks were allowed to be broader than the inner ones. The areas were constrained to scale 3:2:1:1:2:3 in the sextets, as expected for a random absorber. The result from this "three sextet model" is given in Table S2 and the fitted spectrum for $\mathrm{PrFe}_{2/3}\mathrm{Mo}_{1/3}\mathrm{O}_3$ is shown in Fig. 4. To describe the obtained spectra one needs a correlation between center shifts CS and magnetic hyperfine fields *B*. The quadrupole shifts were small and could be neglected in this aspect. Furthermore, a correlation between magnetic fields and quadrupole shifts will not give asymmetric profiles. It is obvious that an increased center shift is correlated to a decreased magnetic field. It is reasonable to assume that these variations in CS and *B* are due to variation in number of Fe and Mo atoms in the nearest surroundings to the Mössbauer atoms. Mössbauer measurements at room temperature of pure $Ln\mathrm{FeO}_3$ Ln = La, Ce, Pr, and Nd show only one symmetrical sextet having typically CS $\approx$ 0.37 mm/s and $B \approx$ 51–53 T [48–51], thus one can assume that the sextets showing higher CS and lower *B* values originate from Fe atoms having more Mo atoms in the nearest surroundings. The different *Ln* elements do not seem to influence the Mössbauer atoms in different ways. The achieved CS and B values are in a good agreement with results reported by Zaripova *et al.* [52] and clearly indicate that all iron atoms are in high spin ferric states, i.e., with valence +3.

E. NPD studies

Refinements of the nuclear and magnetic structure of $Ln\mathrm{Fe}_{2/3}\mathrm{Mo}_{1/3}\mathrm{O}_3$ were performed from NPD patterns obtained at room temperature. Examination of the diffraction patterns for all studied samples confirmed that the *Pnma* symmetry is retained at low temperatures (see Fig. 5). The main crystallographic parameters and the reliability factors obtained after the nuclear and magnetic fits are included in Table S3. Standard deviations of atomic positions and thermal parameters were less than 0.002 Å and 0.03 Å^2, respectively. For comparison, the compositions obtained from EDS analysis are included in Table I. Figure 6 shows the final results of the Rietveld refinements for the Ce compound at different temperatures (see Figs. S1–S3 for corresponding plots concerning the Nd, Pr, and La compounds). There is no indication from the diffraction patterns of any structural phase transition between 4 and 600 K.

The variation of the lattice parameters and unit cell volumes as a function of the effective ionic radii of Ln^{+3} cations (r_{Ln}) (for coordination number 8) is shown in Fig. S4. The standard deviation values of lattice parameters were below 5×10^{-4} Å.

For the structure with *Pnma* symmetry the lattice parameter *c* is most sensitive to the octahedral tilting distortion, while the *a* parameter is relatively insensitive to such a distortion [53]. Thus, changes in the *c* parameter reflect the magnitude

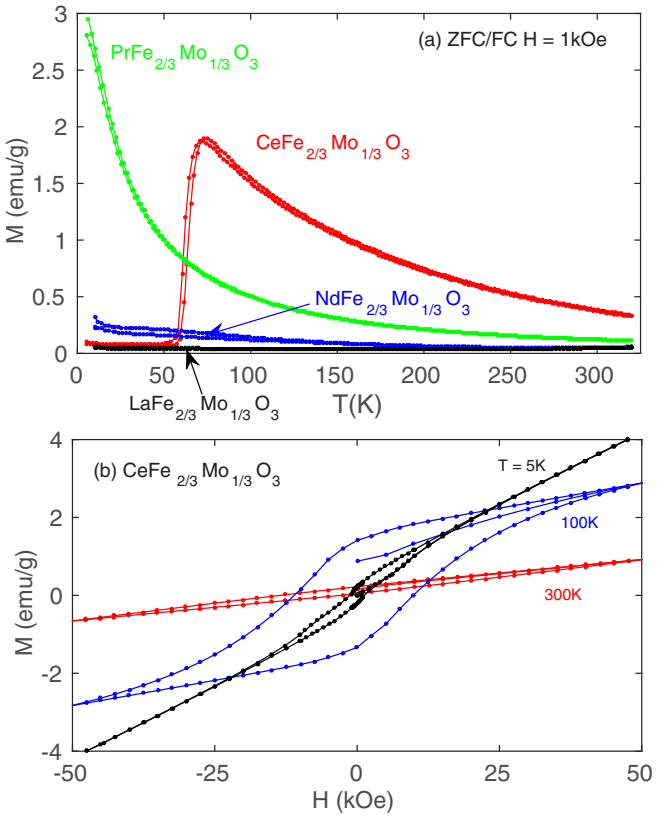

FIG. 3. (Color online) (a) Field-cooled and zero-field-cooled magnetization curves recorded under a magnetic field H = 1 kOe for all samples. (b) Magnetic field dependence of the magnetization for $CeFe_{2/3}Mo_{1/3}O_3$ at T = 5, 100 and 300 K.

of the octahedral tilting distortion, whereas changes in the a parameter serve as a good indicator of the magnitude of the cooperative Jahn-Teller (JT) distortion [54].

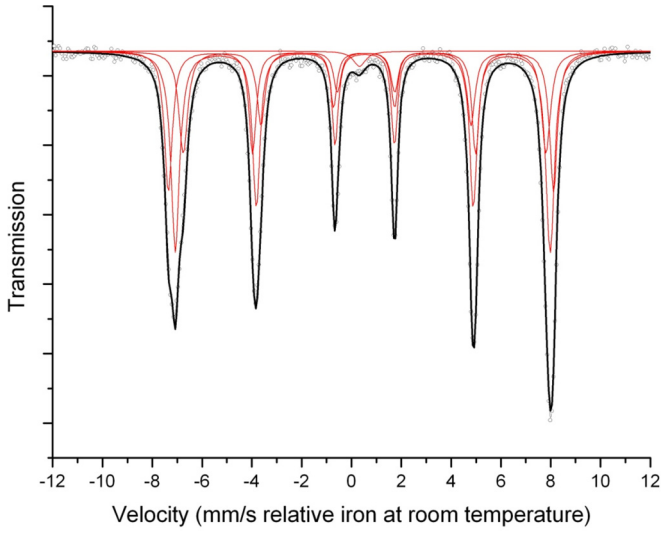

FIG. 4. (Color online) Mössbauer spectrum of $PrFe_{2/3}Mo_{1/3}O_3$ recorded at room temperature. The dots are the measured spectrum, the thin lines are the fitted three sextets and one singlet. The stronger line is the total sum of the fitted functions. See main text for more information about model considered.

Compared to the parent compounds $LnFeO_3$, there is a successive increase of the unit cell dimensions in Mo-doped samples, due to the replacement of high-spin Fe^{3+} ions with slightly larger Mo^{3+} ions. Also, the lattice parameters b and c and unit cell volume of $LnFe_{2/3}Mo_{1/3}O_3$ decrease with decreasing size of the Ln^{+3} ions. This decrease is accompanied by an increase of the structural distortion of the perovskite structure. The lattice parameters of all samples increase smoothly as the temperature is increased. However, just across T_N there seem to occur some extra expansion compared to only a linear thermal expansion. This indicates a weak magnetoelastic coupling in $LnFe_{2/3}Mo_{1/3}O_3$ similar to that observed in some other perovskites [31,55,56]. The point group of orthorhombic $LnFe_{2/3}Mo_{1/3}O_3$, mmm, does not allow piezoelectricity [57], and Fe^{3+} has no positional degree of freedom. However, magnetostriction is allowed by this symmetry and magnetoelastic coupling can cause the observed nonlinearity in the thermal expansion of $LnFe_{2/3}Mo_{1/3}O_3$.

Geometrical parameters characterizing the crystal structure of $LnFe_{2/3}Mo_{1/3}O_3$ were calculated and given in Table II. For example, the orthorhombic distortion $s = (a - c)/(a + c)$ increases with the decrease of the Ln radius, r_{Ln}, while the tolerance factor $t = (r_A + r_O)/\sqrt{2}(r_B + r_O)$ decreases accordingly (cf. Table I), indicating that the lattices become more distorted with decreasing r_{Ln}. The tolerance factor t being smaller than unity also means that the FeO_6 octahedron has to tilt to be accommodated in the lattice matrix.

The perovskite structure can essentially experience three different types of distortions: distortions of the BO_6 octahedral units, displacement of the B cation within the octahedron, and tilting of the essentially rigid BO_6 octahedron [58]. The third and most common distortion, tilting of the BO_6 octahedra, can be viewed as arising from differences in the bonding requirements of the A and B cations. In the case of s.g. *Pnma* (tilt system $a^-b^+c^-$) there are two possibilities to calculate the tilting angles. The first is from the lattice parameters as described in Ref. [59]. The tilts about the cubic [101] and [010] axis are given by θ and φ, respectively, calculated from the expressions $\cos\theta = c/a$ and $\cos\varphi = \sqrt{2}c/b$. However, if the BO_6 octahedra are not perfectly rigid, the tilt angles are more correctly estimated from the atomic coordinates [60,61]. In our case the octahedral tilt angles can be obtained from the displacement of the equatorial O(2) anions from position (1/4,0,3/4) to $(1/4 + u, w, 3/4-v)$. The in-phase tilting occurs about the b axis and the tilt angle is given by $\tan\varphi \sim 4\delta$, where δ is taken as the average shift along the x and z axes $(u + v)/2$. The out-of-phase tilt is about the [101] axis and is calculated by $\tan\theta \sim 4\sqrt{2}\,w$. Our calculations indicated that these two methods give different values, and those calculated using the refined atomic coordinates are typically up to 4–5° larger than those calculated from the lattice parameters alone. This clearly indicates that the octahedral distortions contribute to the tilts. It was found that the tilt angles are reduced as the Ln^{3+} size is increased but remain essentially constant with changing temperature down to 4 K (see Table II). At room temperature, the magnitude of the tilt in the $LnFe_{2/3}Mo_{1/3}O_3$ samples is somewhat greater than those observed for the corresponding undoped $LnFeO_3$ compounds. Considering only structural properties, the effects of doping Mo in $LnFeO_3$ can be summarized as

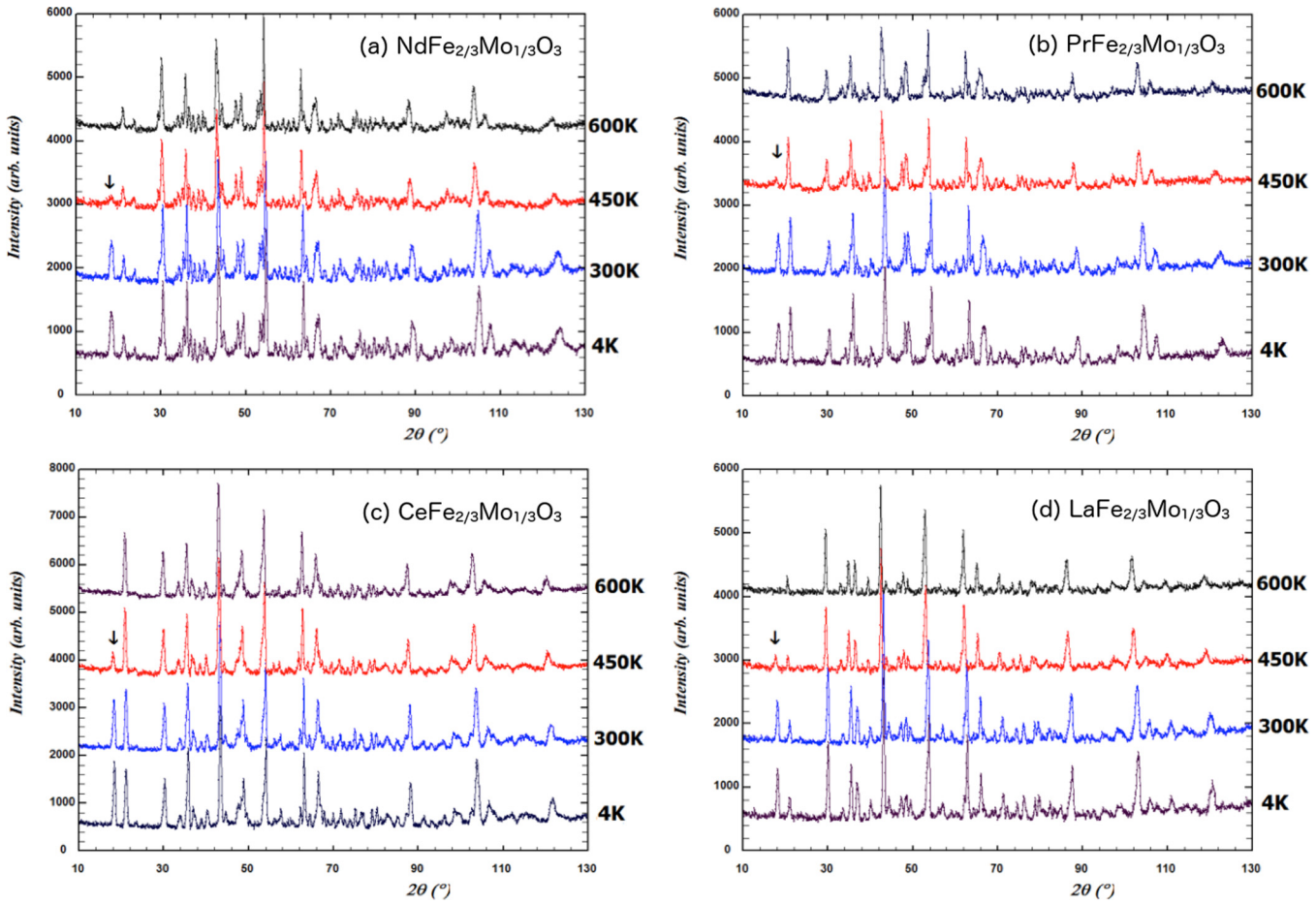

FIG. 5. (Color online) Thermal evolution of the NPD powder patterns for $Ln\mathrm{Fe}_{2/3}\mathrm{Mo}_{1/3}\mathrm{O}_3$ perovskites: (Ln = Nd (a), Pr (b), Ce (c), La (d)).

an increase in octahedral tilt but a decrease in the octahedral deformation.

To gain a full understanding of the structural properties and valence states of the various cations, the IVTON software was employed to perform polyhedral analyses of the structure. The coordination spheres of the A and B cations were characterized, and bond lengths and displacements of the cations from the centers of the coordination polyhedra were obtained. The obtained results are given in Table III. Bond valence sum (BVS) calculations were performed using the parameters R_0 and B tabulated in FULLPROF for Ln^{+3}, Fe^{3+}, and Mo^{+6} cations (there is no data for other ionic states of Mo). Only eight Ln-O bond distances were taken into account since the large tilting angles make it impossible to consider all 12 O^{2-} ions in the first coordination sphere. The obtained BVS values for Ln and Fe are close to the expected values of 3.0 for both cations (see Table III). The derived BVS value for Mo is near 4.0, and this discrepancy in comparison to the expected value +3, which follows from the valence balance in $Ln\mathrm{Fe}_{2/3}\mathrm{Mo}_{1/3}\mathrm{O}_3$, can be attributed to using R_0 and B values for Mo^{+6} instead of the unavailable Mo^{3+} in the BVS calculations. Several examples of disagreement between the postulated and calculated oxidation state are given in Refs. [62,63] where the oxidation state of some cations apparently is incorrectly assigned. Considering these limitations of BVS calculations and the charge balance for our stoichiometric chemical formula, we assign the valence +3 to the Mo cations of $Ln\mathrm{Fe}_{2/3}\mathrm{Mo}_{1/3}\mathrm{O}_3$.

F. Magnetic structure

The thermal evolution of the NPD patterns is shown in Figs. 5(a)–5(d). Strong changes occur below T_N, which corresponds to the magnetic transition. Below this temperature, the intensity of the several Bragg peaks strongly increases due to an additional magnetic contribution. No additional magnetic reflections appeared below T_N. All the diffraction peaks that contained a magnetic scattering contribution could be indexed by the chemical unit cell, i.e., with the propagation vector k = (0, 0, 0). To determine the possible magnetic arrangements based on symmetry considerations, it was convenient to consider the crystal structure of $Ln\mathrm{Fe}_{2/3}\mathrm{Mo}_{1/3}\mathrm{O}_3$ with Ln and Fe/Mo sublattices, without the nonmagnetic oxygen ions for simplicity. In the following, the Fe/Mo sublattice is simply referred to as the Fe sublattice and the average magnetic moment on B site as the Fe^{3+} moment.

To describe the spin couplings and configurations, we use the notation for spins in a pseudocubic lattice commonly used for perovskite structures [64,65]. Representational analysis performed for the Fe spins with BASIREPS for the *4a* Wyckoff site of s.g. *Pnma* revealed *AxGyCz, GxAyFz, CxFyAz*, and *FxCyGz* as possible ordering models (irreducible representations

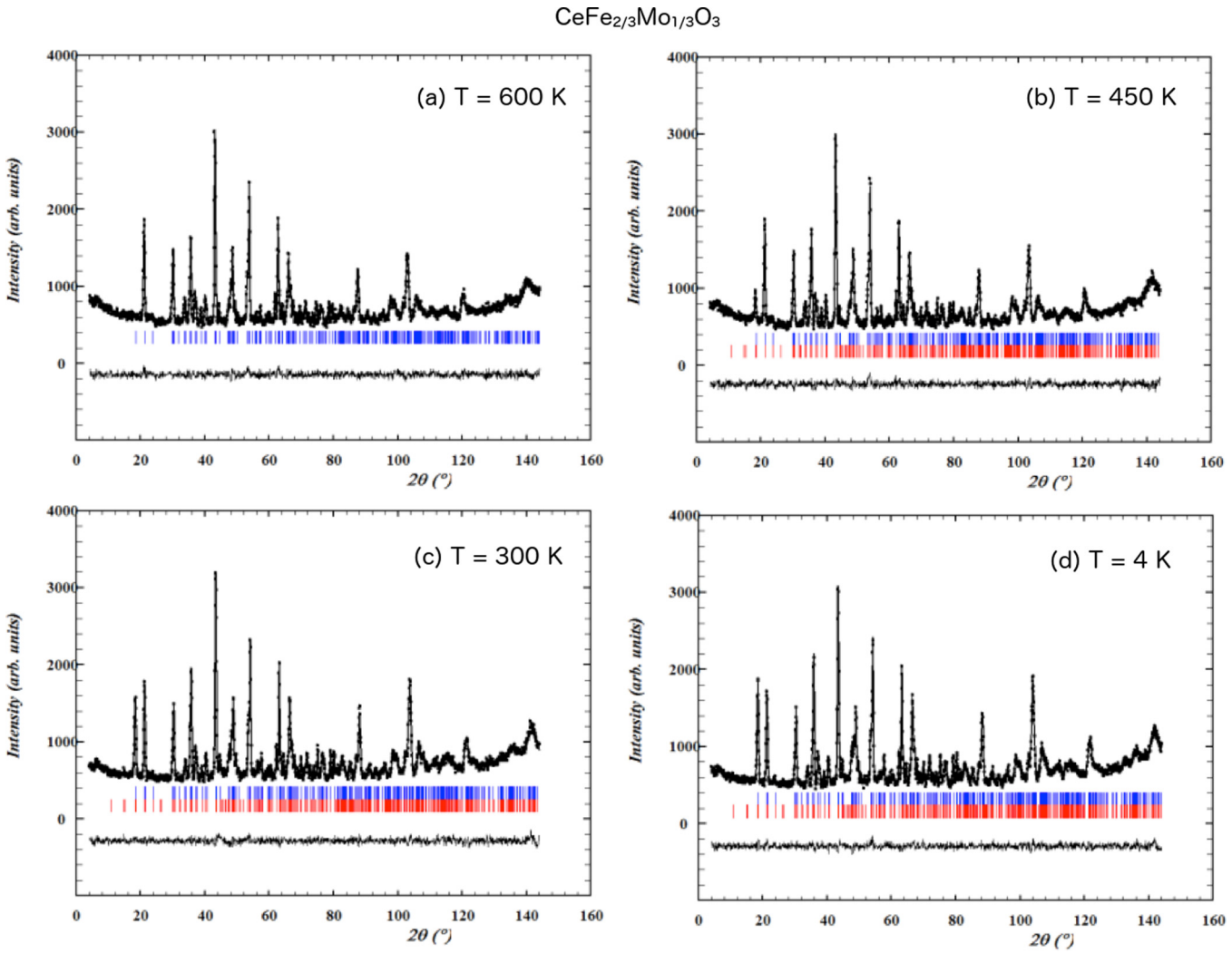

FIG. 6. (Color online) Observed (dots), calculated (full line), and difference (bottom) NPD Rietveld profiles for $CeFe_{2/3}Mo_{1/3}O_3$ at different temperatures: (a) 600 K, (b) 450 K, (c) 300 K, (d) 4 K. The series of tick marks correspond to the allowed Bragg reflections for the nuclear (upper set of tick marks) and magnetic (lower set of tick marks) contributions.

TABLE II. Selected bond distances of $LnFe_{2/3}Mo_{1/3}O_3$ from NPD powder refinements at different temperatures, an ortorhombic distortion (s) and tilting angles for the orthorhombic perovskites: $s = (a-c)/(a+c)$, Θ–tilting angle around $[101]_p$, φ–tilting angle around $[010]_p$,

Phase		Nd				Pr				Ce				La			
T,K		4	295	450	600	4	295	450	600	4	295	450	600	4	295	450	600
Ln	O1	2.322	2.330	2.336	2.340	2.344	2.329	2.382	2.391	2.354	2.370	2.378	2.373	2.377	2.387	2.389	2.421
	O1	2.410	2.427	2.439	2.452	2.448	2.469	2.436	2.440	2.490	2.489	2.490	2.502	2.524	2.538	2.551	2.586
	O2 × 2	2.379	2.378	2.376	2.378	2.398	2.408	2.405	2.405	2.422	2.426	2.419	2.424	2.452	2.458	2.461	2.434
	O2 × 2	2.633	2.630	2.644	2.643	2.653	2.678	2.644	2.653	2.669	2.669	2.677	2.682	2.703	2.708	2.709	2.704
	O2 × 2	2.708	2.723	2.725	2.740	2.724	2.722	2.739	2.751	2.737	2.747	2.749	2.762	2.741	2.745	2.782	2.785
Fe	O1 × 2	2.028	2.031	2.038	2.044	2.024	2.026	2.036	2.043	2.026	2.029	2.037	2.045	2.034	2.036	2.040	2.056
	O2 × 2	2.038	2.038	2.049	2.053	2.039	2.039	2.047	2.046	2.032	2.037	2.039	2.046	2.034	2.040	2.040	2.040
	O2 × 2	2.047	2.052	2.075	2.077	2.045	2.046	2.063	2.070	2.045	2.044	2.061	2.060	2.041	2.039	2.057	2.062
Fe	Fe	3.902	3.908	3.919	3.928	3.913	3.921	3.931	3.941	3.929	3.959	3.946	3.956	3.953	3.960	3.973	3.982
Fe–O1–Fe		148.3	148.4	148.2	147.8	150.4	150.7	149.6	149.3	151.7	152.0	151.3	150.7	152.7	153.2	153.7	151.0
Fe–O2–Fe		149.0	149.1	147.9	148.2	150.3	150.8	150.0	150.2	151.8	152.1	151.2	151.6	153.6	153.8	153.4	153.8
$s(x10^{-3})$		19	19	18	18	15	15	14	14	10	10	9	9	7	6	5	5
φ		11.6	11.4	12.0	11.9	10.9	10.8	11.2	11.0	10.2	10.1	10.6	10.4	9.8	9.7	9.3	9.9
Θ		14.9	15.0	15.4	15.4	14.6	14.3	14.6	14.5	14.0	14.0	14.1	14.0	12.7	12.6	13.7	12.4

TABLE III. Polyhedral analysis of $Ln Fe_{2/3}Mo_{1/3}O_3$ at different temperatures (δ-cation displacement from the center of the ideal coordination polyhedron, ξ-average bond distance and bond-distance limits, V-polyhedral volume, Δ-polyhedral volume distortion).

Cation		T,K	δ(Å)	ξ (Å)	V(Å^3)	Δ	Valence
Ln (c.n. = 8)	Nd	4	0.255	2.522 + /–0.163	26.34	0.074	
		295	0.257	2.527 + /–0.165	26.48	0.074	2.78(2)
		450	0.243	2.533 + /–0.167	26.75	0.071	
		600	0.245	2.539 + /–0.170	26.91	0.071	
	Pr	4	0.277	2.543 + /–0.161	26.80	0.078	
		295	0.284	2.552 + /–0.164	26.95	0.080	2.85(2)
		450	0.274	2.549 + /–0.154	27.12	0.078	
		600	0.279	2.556 + /–0.161	27.27	0.079	
	Ce	4	0.300	2.563 + /–0.157	27.18	0.085	
		295	0.304	2.568 + /–0.156	27.33	0.086	2.80(2)
		450	0.295	2.570 + /–0.158	27.46	0.083	
		650	0.296	2.576 + /–0.162	27.64	0.084	
	La	4	0.324	2.587 + /–0.151	27.71	0.091	
		295	0.327	2.593 + /–0.148	27.90	0.092	2.75(3)
		450	0.333	2.605 + /–0.158	28.19	0.093	
		600	0.321	2.607 + /–0.159	28.22	0.091	
Fe/Mo (c.n. = 6)	Nd	4	0	2.038 + /–0.008	11.27	0.0007	
		295	0	2.040 + /–0.010	11.32	0.0006	2.81(1)/
		450	0	2.054 + /–0.017	11.55	0.0004	3.96(1)
		600	0	2.058 + /–0.015	11.62	0.0004	
	Pr	4	0	2.036 + /–0.010	11.25	0.0004	
		295	0	2.037 + /–0.009	11.26	0.0003	2.83(1)/
		450	0	2.049 + /–0.012	11.46	0.0006	3.99(1)
		600	0	2.053 + /–0.013	11.53	0.0009	
	Ce	4	0	2.034 + /–0.009	11.22	0.0002	
		295	0	2.037 + /–0.007	11.26	0.0002	2.84(1)/
		450	0	2.046 + /–0.012	11.41	0.0003	3.99(1)
		600		2.050 + /–0.008	11.49	0.0004	
	La	4	0	2.036 + /–0.004	11.26	0.0003	
		295	0	2.038 + /–0.002	11.28	0.0002	2.82(1)/
		450	0	2.046 + /–0.009	11.41	0.0003	3.98(1)
		600	0	2.053 + /–0.010	11.52	0.001	

Γ_1, Γ_3, Γ_5, and Γ_7, respectively). Similar analysis performed for the *Ln* cations showed that for the *4c* Wyckoff site the magnetic representation decomposes in terms of eight possible irreducible representations: $\Gamma = \Gamma_1 + 2\Gamma_2 + 2\Gamma_3 + \Gamma_4 + \Gamma_5 + 2\Gamma_6 + 2\Gamma_7 + \Gamma_8$. Only the variants that are allowed for both the *Ln* and the Fe sites were considered, which immediately narrowed down the list of possible solutions.

Data examination showed that the best magnetic model unambiguously was Γ_7 $FxCyGz$ (Shubnikov group Pn'm'a). The derived structure is best described as G-type antiferromagnetic (Fe spins along the *b* axis with some possible canting along *x* and *z*). By the symmetry, the Fe spin can be oriented along three possible directions, but *Ln* only in 2 (*x* and *z*). No significant magnetic contribution from the Ln sublattice was registered down to 4 K in the NPD patterns for all compounds. The observed, calculated, and difference patterns for the final refinements are shown in Fig. 6 for the Ce compound (for other compounds, see Figs S1–S3). The magnetic structure of Nd, Pr, and La is that of a G-type antiferromagnet with all Fe^{3+} cations coupled antiparallel to their six nearest neighbors and all spins being aligned along the *b*-direction. The values of the refined magnetic moments of Fe^{+3} at different temperatures are given in Table S3. At 4 K, the moment reaches a value close to 5 μ_B (see Table S3 for actual values). Fe^{3+}, and Mo^{3+} are expected to carry 5 μ_B and 3 μ_B, respectively. Considering a 2/3:1/3 ratio between Fe^{3+} and Mo^{3+}, the average magnetic moment on B site should be about 4.3 μ_B, in agreement with the obtained value.

The above model was valid also for the Ce sample but only at 300 K. It was found that the magnetic structure at 4 K again corresponds to a G-type structure, but in this case the spins are oriented along the *a*-direction (Γ_1 $AxGyCz$, Shubnikov group Pnma). The Rearrangement of intensity from the (110) to the (011) reflection as the magnetic moments change orientation is illustrated in Figure 7, together with illustrations of the magnetic structure at 4 and 300 K. The magnetic measurements confirm that a magnetic transition of some kind occurs at about 70 K (see Figure 3). Reorientation of the magnetic moments of Fe^{+3} has earlier been observed in $NdFeO_3$ [25] and $CeFeO_3$ [27]. In our data on $Ln Fe_{2/3}Mo_{1/3}O_3$ such an effect was only observed for the Ce based compound.

IV. DISCUSSION

The polyhedral volume ratio V_A/V_B measures the size mismatch between the AO_{12} and BO_6 polyhedra in the

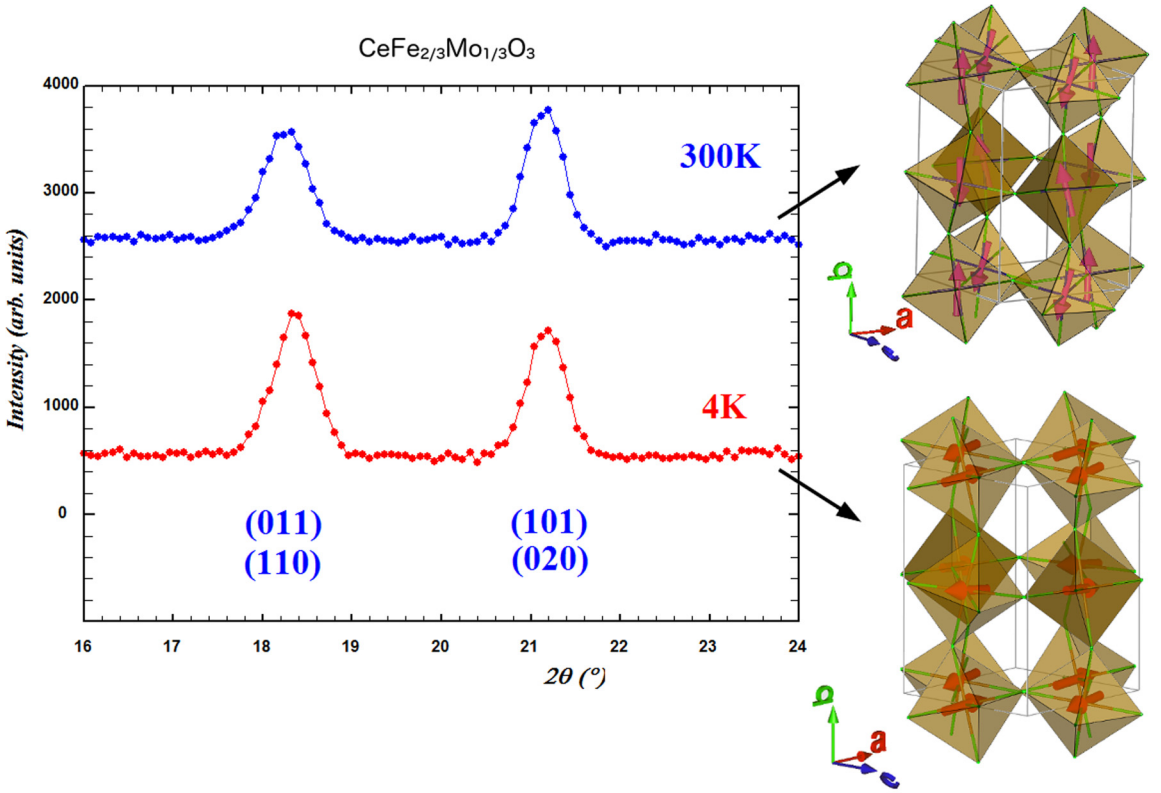

FIG. 7. (Color online) Comparison of the long angle reflections of the NPD diffractograms of $CeFe_{2/3}Mo_{1/3}O_3$ at 300 K and 4 K; the corresponding crystal and magnetic structures are sketched beside each set of data. Fe/Mo spins locate at the center of the octahedron. The arrows show the different direction of Fe/Mo magnetic moments.

perovskite structure. V_A/V_B is equal to 5.0 in the absence of octahedral tilting and decreases with increasing octahedral tilting [61,66]. V_A/V_B ratios in $LnFe_{2/3}Mo_{1/3}O_3$ were here found to be close to 5 (note that in Table III, V_A was estimated for a smaller coordination, 8 instead of 12 as in e.g. [19]). Also, V_A was found to increase with increasing size of Ln^{3+} cation, whereas V_B remains essentially constant.

The Ln^{3+} cations are displaced in the xz-plane in the *Pnma* structure. These antipolar displacements [67] of the rare-earth cation from the high-symmetry position becomes smaller as r_{Ln} increases. With increasing temperature the displacement of the Ln^{3+} ions decreases, but remains non-zero above T_N.

The ortorhombically-distorted $LnFe_{2/3}Mo_{1/3}O_3$ structure is a three-dimensional network of tilted and deformed corner-sharing FMO_6 octahedra (FM = Fe or Mo) with the larger Ln^{3+} cations filling the cavities between eight FMO_6 octahedra. The Jahn–Teller distortion of the FMO_6 octahedra produces three pairs of FM–O bonds. One pair (FM–O_1) is along the *b* axis and the other two pairs lie in the *ac* plane with one of FM–O_2 bonds being long and the other being short as shown in Table II. The tilts of the FMO_6 octahedra yield FM–O_2–FM tilting angles in the ac plane and FM–O_1–FM tilting angles along the *b* direction. As seen in Table II the FM–O_1 bond along the *b* axis is more affected by changes of the Ln^{3+} size than the two FM–O_2 bonds in the ac plane. The general trend is that the FM–O–FM bond angles increase with increasing r_{Ln}.

The magnetic interaction of $LnFeO_3$ is dominated by the superexchange of the Fe–O–Fe interaction, which leads to antiferromagnetic ordering with high Néel temperatures of order 700 K [15–19,68]. The same exchange mechanism is valid for $LnFe_{2/3}Mo_{1/3}O_3$, although, the corresponding transition temperatures are about 250 K lower. This dramatic decrease is primarily a consequence of different spin sizes and d-electron distributions of Fe^{3+} compared to Mo^{3+}. Shortening of the Fe–O bond distance and increase of the Fe–O–Fe bond angle increase the superexchange and thus T_N of $LnFeO_3$. The decreasing radius of rare earth ions enhances the tilt of the FeO_6 octahedron and leads to a decrease of Fe–O–Fe bond angle and according to the Goodenough–Kanamori rule [69,70], the overlap integral is the largest when the Fe–O–Fe bond angle is 180° and becomes smaller when the Fe–O–Fe bond angle decreases from 180°. The two superexchange angles decrease gradually with the decrease of r_{Ln} and thus also T_N of $LnFe_{2/3}Mo_{1/3}O_3$ is expected to decrease correspondingly.

A correlation between T_N and the distortion angle θ is established in [23] and is confirmed by our current results. Figure 8 shows the variation of T_N with bond and distortion angles using data from Table III and T_N = 467, 470, 480 and 490 K for Nd, Pr, Ce and Nd doping from this investigation together with corresponding data for $LnFeO_3$ and T_N values of 687, 707, 719 and 740 K, respectively, obtained from literature [18,19].

$LnFe_{2/3}Mo_{1/3}O_3$ possesses a weak ferromagnetic moment as a result of spin canting from the ideal G-type antiferromagnetic ordering as a consequence of the tilted Fe–O–Fe interaction pathways and the magnetocrystalline anisotropy. Also, as the temperature is lowered, the rare earth ions become

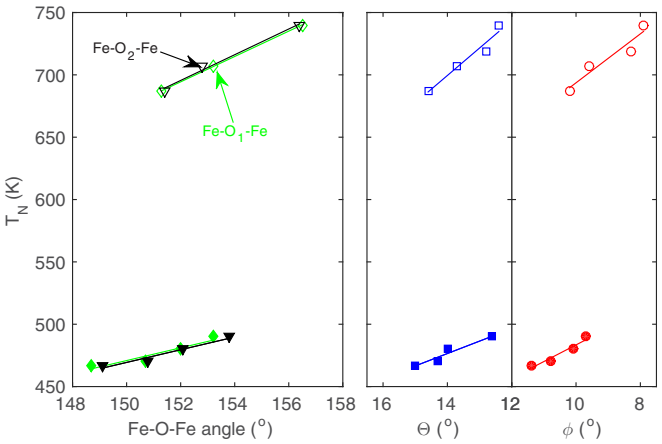

FIG. 8. (Color online) Variation of T_N of pure and Mo-doped samples with (right) the Fe–O–Fe bond angles and (left) tilting angles Θ and Φ estimated at room temperature. Filled symbols represent Mo-doped samples, using crystallographic data extracted from the present NPD data measured at 295 K, while open symbols represent data extracted from XRPD data at room-temperature from the literature [18,19] on the undoped compounds. No data was found for pure Ce compound. Linear fits of each dataset are included, as guides to the eye.

increasingly polarized, their effective anisotropy increases, and the antiferromagnetic structure may undergo a spin reorientation transition in which the Fe/Mo spins reorient from being essentially parallel to the *b*-axis to become oriented along the a-axis. Such a reorientation was in this investigation only observed in $CeFe_{2/3}Mo_{1/3}O_3$.

It is in this context worth to note that the temperature of the magnetic phase transition (T_N) for $LaBO_3$ and $La(B_{2/3}Mo_{1/3})O_3$ with different 3d magnetic cations such as B = Fe, Mn, Co is very much lower for Mn and Co based compounds than for the iron containing compounds (following [71,72] T_N = 143 K for Co and 89 K for Mn).

V. CONCLUSIONS

Stoichiometric $LnFe_{2/3}Mo_{1/3}O_3$ (Ln = Nd, Pr, Ce and La) polycrystalline samples were synthesized. The structural and magnetic properties of the samples were investigated in detail in order to clarify the structure-physical property relationship in this system.

The substitution of Fe^{3+} by Mo^{3+} cations depresses the antiferromagnetic ordering temperature significantly. This is primarily a consequence of different spin sizes and electron distributions of Fe^{3+} compared to Mo^{3+}. The orthorhombic distortion and tilting angles decrease with increasing size of the Ln^{3+} cation, as the Fe–O and Fe-Fe bond lengths, as well as Fe–O–Fe bond angles increase. It was demonstrated that these $LnFe_{2/3}Mo_{1/3}O_3$ samples order in a G-type antiferromagnetic structure.

The valence state of Fe was by Mossbauer spectroscopy found to be Fe^{+3}. Interestingly, our results indicate that the valence state of Mo is +3 in all investigated $LnFe_{2/3}Mo_{1/3}O_3$ compounds. Another interesting finding is that a spin reorientation at low temperature is observed in one of the compounds: $CeFe_{2/3}Mo_{1/3}O_3$.

ACKNOWLEDGEMENTS

Financial support from the Swedish Research Council (VR), the Göran Gustafsson foundation, the Swedish Foundation for International Cooperation in Research and Higher Education (STINT) and the Russian Foundation for Basic Research is gratefully acknowledged. P.B. acknowledges support from the infrastructure CANAM of the NPI ASCR Rez supported through MSMT Project No. LM2011019.

[1] S. P. N. Nair and P. Murugavel, *Comprehensive Inorganic Chemistry II (Second Edition): From Elements to Applications*, Volume 4: Solid-State Materials (Elsevier, 2013), pp. 47–72.
[2] J. Zhang and H. Li, *Perovskite: Crystallography, Chemistry and Catalytic Performance* (Nova Science Publishers, 2013), p. 243.
[3] M. Dawber, K. M. Rabe, and J. F. Scott, Rev. Mod. Phys. **77**, 1083 (2005).
[4] N. A. Spaldin and M. Fiebig, Science **309**, 391 (2005).
[5] J. M. Rondinelli and N. A. Spaldin, Adv. Mater. **23**, 3363 (2011).
[6] N. A. Hill, J. Phys. Chem. B **104**, 6694 (2000).
[7] Y. Nishihata, J. Mizuki, T. Akao, H. Tanaka, M. Uenishi, M. Kimura, T. Okamoto, and N. Hamada, Nature **418**, 164 (2002).
[8] P. V. Hendriksen, P. H. Larsen, M. Mogensen, F. W. Poulsen, and K. Wiik, Catal. Today **56**, 283 (2000).
[9] G. Martinelli, M. C. Carotta, M. Ferroni, Y. Sadaoka, and E. Traversa, Sensor Actuator B-Chem. **55**, 99 (1999).
[10] P. Ciambelli, S. Cimino, L. Lisi, M. Faticanti, G. Minelli, I. Pettiti, and P. Porta, Appl. Catal. B **33**, 193 (2001).
[11] Z. Y. Zhao, X. M. Wang, C. Fan, W. Tao, X. G. Liu, W. P. Ke, F. B. Zhang, X. Zhao, and X. F. Sun, Phys. Rev. B **83**, 014414 (2011).
[12] Y. Tokunaga, Y. Taguchi, T. Arima, and Y. Tokura, Nat. Phys. **8**, 838 (2012).
[13] Y. Tokunaga, N. Furukawa, H. Sakai, Y. Taguchi, T. Arima, and Y. Tokura, Nat. Mater. **8**, 558 (2009).
[14] S. Acharya, J. Mondal, S. Ghosh, S. K. Roy, and P. K. Chakrabarti, Mater. Lett. **64**, 415 (2010).
[15] *Landolt-Börnstein*, edited by H. P. J. Wijn, Numerical Data and Functional Relationships in Science and Technology *Group III*, Vol. 27f3 (Berlin: Springer, 1994).
[16] S. Hu, L. Chen, Y. Wu, L. Yu, X. Zhao, S. Cao, J. Zhang, and W. Ren, Chin. Sci. Bull. **59**, 5170 (2014).
[17] R. L. White, J. Appl. Phys. **40**, 1061 (1969).
[18] Z. Zhou, L. Guo, H. Yang, Q. Li, and F. Ye, J. Alloys Compd. **583**, 21 (2014).
[19] S. A. Ivanov, R. Tellgren, F. Porcher, T. Ericsson, A. Mosunov, P. Beran, S. K. Korchagina, P. Anil Kumar, R. Mathieu, and P. Nordblad, Mater. Res. Bull. **47**, 3253 (2012).
[20] J. F. Scott, NPG Asia Mater. **5**, e72 (2013).
[21] E. Bousquet and N. Spaldin, Phys. Rev. Lett. **107**, 197603 (2011).
[22] M. Lezaic and N. A. Spaldin, Phys. Rev. B **83**, 024410 (2011).

[23] J. S. Zhou and J. B. Goodenough, Phys. Rev. B **77**, 132104 (2008).

[24] T. Yamaguchi, J. Phys. Chem. Solids **35**, 479 (1974).

[25] W. Slawinski, R. Przenioslo, I. Sosnowska, and E. Suard, J. Phys.: Condens. Matter **17**, 4605 (2005).

[26] J. H. Lee, Y. K. Jeong, J. H. Park, M. A. Oak, H. M. Jang, J. Y. Son, and J. F. Scott, Phys. Rev. Lett. **107**, 117201 (2011).

[27] S. J. Yuan, Y. M. Cao, L. Li, T. F. Qi, S. X. Cao, J. C. Zhang, L. E. DeLong, and G. Cao, J. Appl. Phys. **114**, 113909 (2013).

[28] G. W. Durbin, C. E. Johnson, L. A. Prelorendjo, and M. F. Thomas, J. Phys. Colloques **37**, C6-621 (1976).

[29] E. K. H. Salje, Annual Rev. Mater. Res. **42**, 265 (2012).

[30] E. K. H. Salje, *Phase Transition in Ferroelastic and Co-Elastic Crystals* (Cambridge University Press, Cambridge, UK, 1993).

[31] S. M. Selbach, J. R. Tolchard, A. Fossdal, and T. Grande, J. Sol. State Chem. **196**, 249 (2012).

[32] M. Parra-Borderías, F. Bartolomé, J. A. Rodríguez Velamazán, and J. Bartolomé, J. Phys.: Condens. Matter **23**, 046003 (2011).

[33] N. Kimizuka, A. Yamamoto, H. Ohashi, T. Sugihara, and T. Sekine, J. Solid State Chem. **49**, 65 (1983).

[34] G. V. Bazuev, G. P. Shveikin, and O. V. Makarova, Izv. Akad. Nauk SSSR, Neorg. Mater. **22**, 434 (1986).

[35] G. V. Bazuev, V. G. Zubkov, and G. P. Shveikin, Russ. J. Inorg. Chem. **41**, 2000 (1996).

[36] See Supplemental Material at http://link.aps.org/supplemental/10.1103/PhysRevB.91.094418.

[37] D. G. Rancourt, A. M. McDonald, A. E. Lalonde, and J. Y. Ping, Amer. Mineral. **78**, 1 (1993).

[38] K. Lagarec and D. G. Rancourt, Nucl. Instr. Meth. B **129**, 266 (1997).

[39] J. Rodrigues-Carvajal, Physica B **192**, 55 (1993).

[40] R. Lelieveld and D. J. W. Ijdo, Acta Cryst. B **36**, 2223 (1980).

[41] Y. Zhao, D. J. Weidner, J. B. Parise, and D. E. Cox, Phys. Earth Planet. Inter. **76**, 1 (1993).

[42] N. E. Brese and M. O´Keefe, Acta Cryst. B **47**, 192 (1991).

[43] I. D. Brown in *Computer Modeling in Inorganic Crystallography* (Academic Press, San Diego, 1997), pp. 23–53.

[44] T. B. Zunic and I. Vickovic, J. Appl. Cryst. **29**, 305 (1996).

[45] S. Geller and E. A. Wood, Acta Cryst. **9**, 563 (1956).

[46] J. Navarro, L. L. Balcells, F. Sandiumenge, M. Bibes, A. Roig, B. Martínez, and J. Fontcuberta, J. Phys.: Condens. Matter **13**, 8481 (2001).

[47] M.-R. Li, D. Walker, M. Retuerto, T. Sarkar, J. Hadermann; P. W. Stephens, M. Croft, A. Ignatov, C. P. Grams, J. Hemberger, I. Nowik, P. Shiv Halasyamani, T. Thao Tran, S. Mukherjee, T. Saha Dasgupta, and M. Greenblatt, Angew. Chem. Int. Ed. **53**, 10774 (2014).

[48] F. J. Berry, J. R. Gancedo, J. F. Marco, and X. Ren, Hyp. Interact. (C) **5**, 273 (2002).

[49] M. Robbins, G. K. Wertheim, A. Menth, and R. C. Sherwood, Phys. Chem. Solids **30**, 1823 (1969).

[50] S. Music, S. Popovic, M. Ristic, and B. Sepiol, J. Mater. Sci. **29**, 1714 (1994).

[51] M. Ristic, S. Popovic, and S. Music, Croat. Chem. Acta **86**, 281 (2013).

[52] L. D. Zaripova, N. V. Boltakova, A. A. Valiullin, and Sh. Bashkirov, Tech. Phys. **50**, 473 (2005).

[53] P. M. Woodward, T. Vogt, D. E. Cox, A. Arulraj, C. N. R. Rao, P. Karen, and A. K. Cheetham, Chem. Mater. **10**, 3652 (1998).

[54] M. W. Lufaso and P. M. Woodward, Acta Cryst. B **60**, 10 (2004).

[55] S. M. Selbach, T. Tybell, M.-A. Einarsrud, and T. Grande, Chem. Mater. **21**, 5176 (2009).

[56] M. Fiebig, J. Phys. D **38**, R123 (2005).

[57] M. E. Lines and A. M. Glass, *Principles and Applications of Ferroelectrics and Related Materials* (Oxford University Press, New York, 2001).

[58] H. D. Megaw, *Crystal Structures — A Working Approach* (W. B. Saunders, Philadelphia, 1973).

[59] B. J. Kennedy, C. J. Howard, and B. C. Chakoumakos, J. Phys.: Condens. Matter **11**, 1479 (1999).

[60] M. A. O'Keefe, B. Hyde, and J. Bovin, Phys. Chem. Miner. **4**, 299 (1979).

[61] I. Qasim, B. J. Kennedy, and M. Avdeev, J. Mater. Chem. A **1**, 13357 (2013).

[62] P. L. Roulhac and G. J. Palenik, Inorg. Chem. **42**, 118 (2003).

[63] J. Frantti, S. A. Ivanov, S. Eriksson, J. Lappalainen, V. Lantto, M. Kakihana, and H. Rundlöf, Ferroelectrics **272**, 51 (2002).

[64] E. Wollan and W. Koehler, Phys. Rev. **100**, 545 (1955).

[65] E. F. Bertaut, Acta Cryst. A **24**, 217 (1968).

[66] R. H. Mitchell, *Perovskites: Modern and Ancient* (Almaz Press, Thunder Bay, Canada, 2002).

[67] N. A. Benedek and C. J. Fennie, J. Phys. Chem. C **117**, 13339 (2013).

[68] M. Eibschutz, S. Shtrikman, and D. Treves, Phys. Rev. **156**, 562 (1967).

[69] J. B. Goodenough, J. Phys. Chem. Solids **6**, 287 (1958).

[70] J. Kanamori, J. Phys. Chem. Sol. **10**, 87 (1959).

[71] G. V. Bazuev, G. P. Shveikin, and O. V. Makarova, Russ. J. Inorg. Chem. **32**, 2550 (1987).

[72] G. V. Bazuev, A. S. Boruhovich, and A. A. Sidorov, Izv. Akad. Nauk SSSR, Neorg. Mater. **25**, 95 (1989).